

Phase diagram of crushed powders

Sébastien Bodard, Olivier Jalbaud, Richard Saurel, Yves Burtshell, and Emmanuel Lapebie

Citation: *Physics of Fluids* **28**, 123301 (2016); doi: 10.1063/1.4968195

View online: <http://dx.doi.org/10.1063/1.4968195>

View Table of Contents: <http://scitation.aip.org/content/aip/journal/pof2/28/12?ver=pdfcov>

Published by the [AIP Publishing](#)

Articles you may be interested in

[The influence of morphology on the low- and high-strain-rate compaction response of CeO₂ powders](#)

J. Appl. Phys. **115**, 123511 (2014); 10.1063/1.4868356

[Predicting the shock compression response of heterogeneous powder mixtures](#)

J. Appl. Phys. **113**, 223513 (2013); 10.1063/1.4810929

[Consolidation of Bi-2223 superconducting powders by spark plasma sintering](#)

J. Appl. Phys. **112**, 113906 (2012); 10.1063/1.4768257

[Universality in phase diagram of \(K , Na \) NbO₃ – MTiO₃ solid solutions](#)

Appl. Phys. Lett. **95**, 092905 (2009); 10.1063/1.3224196

[Phase diagrams of alkali halides using two interaction models: A molecular dynamics and free energy study](#)

J. Chem. Phys. **126**, 024503 (2007); 10.1063/1.2423030

A photograph of a laptop computer with a red cloth draped over its screen and keyboard, symbolizing an unveiling or reveal. The laptop is silver and the red cloth is bright and glossy.

The Unveiling Nears

The new *Physics Today* website will soon be launched. It will be faster, more attractive, and easier to search on all your devices.

PHYSICS TODAY

Phase diagram of crushed powders

Sébastien Bodard,^{1,a)} Olivier Jalbaud,^{2,a)} Richard Saurel,^{1,3,a)}

Yves Burtschell,^{2,a)} and Emmanuel Lapebie^{4,a)}

¹RS2N, 371 Chemin de Gaumin, 83640 Saint Zacharie, France

²Polytech Marseille, 60 rue Joliot Curie, 13013 Marseille, France

³Aix Marseille Université, CNRS, Centrale Marseille, M2P2, Marseille, France

⁴CEA Gramat, 46500 Gramat, France

(Received 23 May 2016; accepted 7 November 2016; published online 1 December 2016)

Compression of monodisperse powder samples in quasistatic conditions is addressed in a pressure range such that particles fragmentation occurs while the solid remains incompressible (typical pressure range of 1–300 MPa for glass powders). For a granular bed made of particles of given size, the existence of three stages is observed during compression and crush up. First, classical compression occurs and the pressure of the granular bed increases along a characteristic curve as the volume decreases. Then, a critical pressure is reached for which fragmentation begins. During the fragmentation process, the granular pressure stays constant in a given volume range. At the end of this second stage, 20%–50% of initial grains are reduced to finer particles, depending on the initial size. Then the compression undergoes the third stage and the pressure increases along another characteristic curve, in the absence of extra fragmentation. The present paper analyses the analogies between the phase transition in liquid-vapour systems and powder compression with crush-up. Fragmentation diagram for a soda lime glass is determined by experimental means. The analogues of the saturation pressure and latent heat of phase change are determined. Two thermodynamic models are then examined to represent the crush-up diagram. The first one uses piecewise functions while the second one is of van der Waals type. Both equations of state relate granular pressure, solid volume fraction, and initial particle diameter. The piecewise functions approach provides reasonable representations of the phase diagram while the van der Waals one fails. *Published by AIP Publishing.* [<http://dx.doi.org/10.1063/1.4968195>]

I. INTRODUCTION

Compression of powders has been widely studied in the kilobar range (Kuo *et al.*, 1980 and Elban and Chiarito, 1986) and at higher pressures in the megabar range (Marsh, 1980 and Fortov *et al.*, 2013) with dynamic shock loading. Dynamic rupture and fragmentation of granular materials have been an intense research area since the pioneer work of Griffith (1921), Mott (1948), Einav (2007a; 2007b), Mott (2006), and Davison *et al.* (2012) and many other researchers.

In this paper, we address the quasi-static compression of initially monodisperse spherical soda-lime glass particles. The (quasi) monodisperse character of the initial bed enables studying the effects of the initial particle size.

The compression of such granular beds exhibits three successive stages. During the first one, the behaviour that is observed corresponds to conventional loading curves reported, for example, in Kuo *et al.* (1980) and Elban and Chiarito (1986) and summarized by a “configuration pressure” equation of state (EOS) (Passman *et al.*, 1984). In this regime, grains deform in the elastic-plastic regime and fragmentation is rare. During this stage, the “granular pressure” (denoted β) increases

^{a)}Electronic addresses: sebastien.bodard@rs2n.eu; olivier.jalbaud@univ-amu.fr; richard.saurel@univ-amu.fr; yves.burtschell@univ-amu.fr; and emmanuel.lapebie@cea.fr

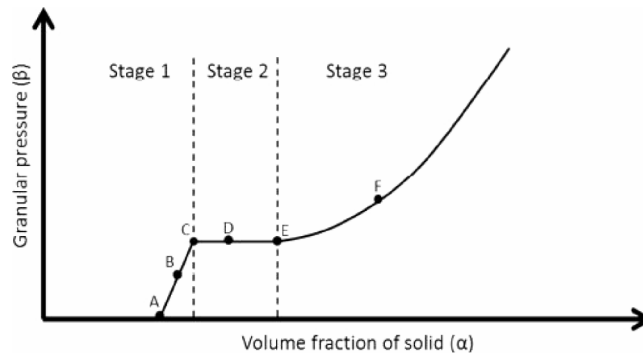


FIG. 1. Typical granular pressure evolution as a function of the volume fraction of solid during a compression test. A: initial granular bed configuration, B: elastic-plastic deformation and reorganisation processes, C: first grain fracture, D: fragmentation at nearly constant granular pressure, E: last grain fracture, F: elastic-plastic deformation and reorganisation of the fragmented powder.

when the solid volume fraction increases too. This granular pressure represents collective intergranular effects during compression due to contacts. Details are given in [Bdzil *et al.* \(1999\)](#) where this pressure is linked to a surface energy and in [Saurel *et al.* \(2010\)](#) where a convenient and accurate EOS formulation is given.

When the compression continues, some critical granular pressure level is reached and the second stage begins. The fragmentation occurs and produces characteristic noise in the experiments. The fragmentation process is continuous with volume decreases and occurs at nearly constant granular pressure, as will be discussed. This particular feature appears to be of prime interest for the study of granular bed fragmentation. Then, at a given compression level, the fragmentation halts and the third compression stage begins. The powder is now polydisperse, made of particles having initial size as well as smaller grains. Its compression curve follows another characteristic curve, quite similar to the one of the first stage. The particle fragmentation is quite rare during this third compression stage.

These three stages are illustrated in Figure 1 and in the author's knowledge has not been reported before.

Compaction of several powder samples made of the same material but with different initial particle sizes enables the determination of a "fragmentation diagram," schematized in Figure 2. It has similarities with isothermal compression of liquid-vapour systems as, for instance, presence of a fragmentation dome (analogue of the saturation dome) and a critical point. When the initial particles diameter is greater than the critical one, the fragmentation is possible and the compaction process follows the three stages described previously. Otherwise no fragmentation occurs and compaction follows the initial characteristic curve (the one of the first stage).

The determination of the fragmentation diagram may be useful for various applications, such as, for example, the building of protection materials against mechanical aggressions or the behaviour of materials during projectile's impact.

II. EXPERIMENTS AND RESULTS

A conventional laboratory press (CBR T0105.1) is used to compress powder samples of a few grams. A steel piston is moved at a velocity of 1.27 mm/min to achieve compression. The compression cell is a steel tube with 24.9 mm inner diameter. The maximal force reached by the press is about 100 kN. Figure 3 illustrates the experimental setup. For each compression test, the height of the sample was measured with a displacement gauge. The applied force (F_a) and the transmitted force (F_t) were recorded at the upper and lower surfaces of the compression chamber, respectively. We found nearly equal forces, meaning quasi-uniform pressure in the granular sample. The transmitted force was measured with a quasi-static load cell, model FLB451 manufactured by

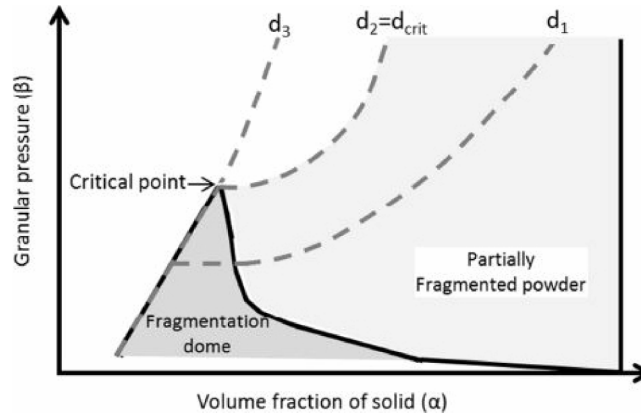


FIG. 2. Schematic representation of the fragmentation diagram. The fragmentation dome is represented by a dark grey area. Three typical compaction paths are shown with dashed grey lines for different initial diameters such that $d_1 > d_2 = d_{\text{crit}} > d_3$. d_{crit} is the critical initial diameter under which no fragmentation happens during granular bed compression.

TEI (Technologies et Equipements Industriels, France). This cell has a force measurement range of 15–50 kN and tolerance 0.5 kN.

Following [Kuo *et al.* \(1980\)](#), the granular pressure β is computed as $\beta = \frac{F_a + F_t}{2\alpha S}$, with S the upper and lower surface area of the sample. The solid volume fraction is computed as $\alpha = m_s / (\rho_s V)$ with m_s the mass of powder in the sample, ρ_s the density of the particle (2500 kg/m³ for soda lime glass), and V the volume of the sample. Seven granular samples of the soda-lime glass have been considered. Their characteristics are summarised in [Table I](#). The experimental compaction curves are presented in [Figure 4\(a\)](#) in the $(\beta - \alpha)$ -plane. Note that the form of the curves is the same in the $(\beta - \rho)$ -plane as $\alpha \rho_s \cong \rho$, the gas density being negligible compared to the solid one. [Figure 4\(b\)](#) shows the liquid-vapour phase change of CO₂ in the $(P - \rho)$ -plane to illustrate the analogy. Obviously any other liquid-vapour substance could be considered as well (H₂O, N₂). Thermodynamics data of CO₂ have been collected from the NIST online library (<http://webbook.nist.gov/chemistry/>).

[Table I](#) provides grains size used in each test and their respective size range. Unfortunately for obvious technical reasons, it has not been possible to deal with perfectly monodisperse granular beds. But each class of particle size is distinct enough from the others to observe the various distinct compression curves shown in [Figure 4\(a\)](#). We believe that particle samples made of single spherical particles would show a clearer slope change when the fragmentation halts, as it is for liquid-vapour systems, where the isotherms in the liquid show abrupt changes with the saturation line.

In the present experiments and analysis, it is assumed that the granular bed contains enough particles in all directions to be considered as a continuum. For Test 1, considering particles of

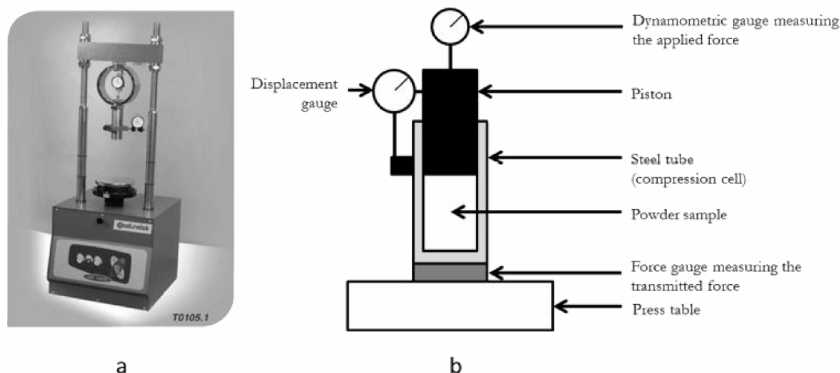


FIG. 3. Representation of the experimental facility: (a) laboratory press, (b) experimental setup.

TABLE I. Characteristics of powder samples (soda lime).

Test	1	2	3	4	5	6	7
Grain size (μm)	2000-3000	1600-2000	850-1000	500-600	355-425	212-250	27-32
Initial mass (g)	8.36	8.36	5.06	5.02	5.02	5.06	5.02
Initial volume (cm^3)	5.82	5.74	3.38	3.29	3.22	3.26	3.38
Approximate number of grains in the compression cell	410	1100	4900	23 000	65 000	310 000	1.4×10^8

average size 2.5 mm (the biggest of the present study), 10 particles are present along the cell diameter, and 6 layers of particles are present in the vertical direction. This cell appeared to be of sufficient size regarding repeatability and coherence of the results of Figure 4(a). For other tests, particles being smaller, the assumption of continuum media is supported.

The accuracy of measurements and data reported in Figure 4(a) are discussed in Section IV.

III. ANALYSIS OF THE EXPERIMENTS

In this section, the experimental data are analysed and the extent of the analogy between fragmentation and liquid-vapour phase diagrams is discussed. First, we focus on the differences between the two phenomena. For liquid-vapour systems, the phase change is reversible and occurs at constant pressure. Powder fragmentation is obviously irreversible. Another noticeable difference is that, for liquid-vapour systems, outside the saturation dome the phase is a pure liquid or a pure gas. For powders, the total fragmentation is never observed and a part of the initial particles remains intact.

For each powder sample, the post fragmentation granular bed consisted in three main classes of particles: intact grains, coarse grains of smaller size (a half to a tenth of the initial grain diameter), and fine dusts. These three classes of particle sizes have been roughly separated and corresponding mass fractions summarized in Figure 5. An example of the three classes of particles collected after a compression test is shown in Figure 6. From Figure 5, it appears that the mass fraction of fragments (dust + coarse) is about 20% for powder samples made of 250 μm initial diameter particles and tends to 70% for big particles (3 mm). A schematic drawing of the observed sample cross section after the final fragmentation is presented in graph (e) of Figure 7. It seemed that fragmented particles were trapped in initial intergranular voids, rendering stress isotropic around particles and preventing further fragmentation.

Knowing the initial and final configuration of the granular bed (graphs (a) and (e) of Figure 7, respectively), the fragmentation process at the grain scale is assumed to follow the steps shown in Figure 7: (a) the initial granular bed is compacted and grains are reorganised, (b) grains are deformed in the elastic-plastic regime, (c) fragmentation appears and the bed becomes polydisperse,

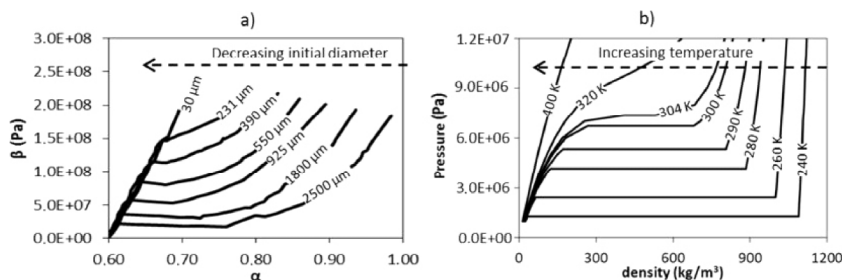


FIG. 4. (a) Phase diagram of pressed granular beds made of glass particles. β represents the granular pressure and α the volume fraction. Lines represent compression curves for the given initial particle diameter. (b) Liquid-gas phase diagram of CO_2 .

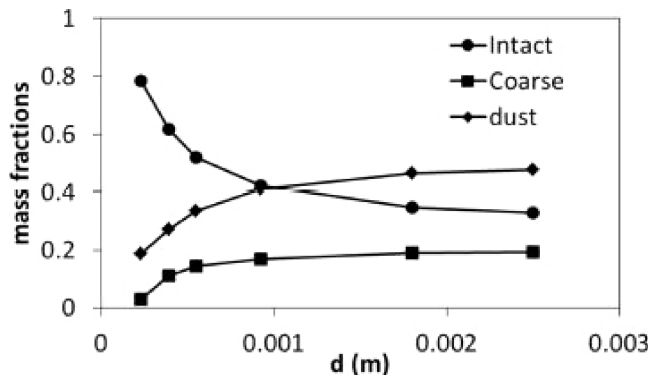


FIG. 5. Mass fractions of the various grain sizes after compression (end of stage 2).

(d) all initial voids are filled with particle fragments and the stress field around particles becomes isotropic, preventing further fragmentation, (e) grains are reorganized and deform again in the elastic-plastic regime.

The amount of fragmented particles as a function of the initial diameter can be qualitatively understood by considering initial intergranular voids. In the case of big particles, the fragmented particles are polydisperse, as large particles break into medium ones that possibly break again and fill intergranular voids. Beds made of smaller particles show narrower polydispersity.

As a result, voids are less effectively filled with particles of small initial size than for larger ones, as already mentioned by [Desmond and Weeks \(2014\)](#). In the limit, small enough particles do not crush at all. Such behaviour is well known in metallurgy through the Hall-Petch law ([Hall, 1951](#) and [Petch, 1953](#)). It expresses grain's hardening increase when size decreases. More precisely, the yield strength increases when size decreases, rendering the harder plastic transition. It results that the plastic flow in small grains is more difficult to reach and consequently the fragmentation follows the same tendency, in agreement with the observations of [Figure 4\(a\)](#). Such behaviour fails however for nanoparticles but is valid for particle sizes of the present study (typically of several microns).

The comparison of the graphs of [Figure 4](#), showing the fragmentation diagram of powders on one hand and the liquid-vapour diagram of CO_2 on the other hand, indicates that the inverse of the initial particle diameter plays similar role as temperature. The temperature is however a thermodynamic variable while the initial diameter is not, making differences in the definition of the latent heat of phase change and fragmentation energy.

Main differences between liquid-vapour and fragmentation diagrams having been discussed, we now examine similarities. Comparing again the graphs of [Figure 4](#), obvious analogies exist between the fragmentation diagram in the $(\beta-\alpha)$ -plane (or in the $(\beta-\rho)$ -plane) and the liquid-vapour diagram in the $(p-\rho)$ -plane. Among these common features, the existence of crush granular pressure appears, as well as the fragmentation dome and critical point (analogues of the saturation pressure, saturation dome, and critical point, respectively). In vapour-liquid systems, the most important

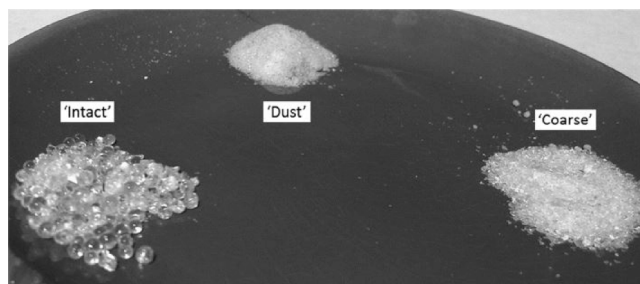


FIG. 6. Photograph of the three main classes of particles collected after compression (Test 1). After approximate separation each class of powder is weighted and the associated proportion is reported in [Figure 5](#).

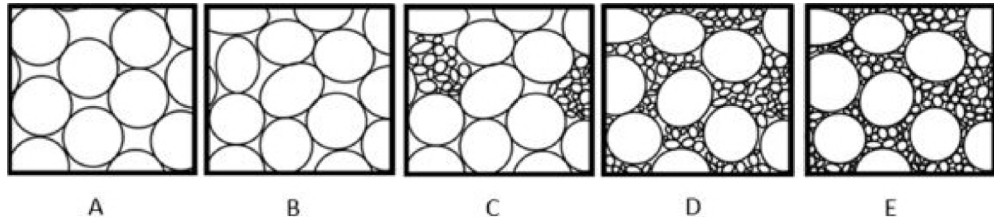


FIG. 7. Schematic representation of the fragmentation process. (a) the initial granular bed is compacted and grains are reorganised, (b) grains are deformed in the elastic-plastic regime, (c) fragmentation appears and the bed becomes polydisperse, (d) all initial voids are filled with particle fragments and the stress field around particles becomes isotropic, preventing further fragmentation, (e) grains are reorganized and deform again in the elastic-plastic regime.

relations are the saturated pressure (P_{sat}), the saturated densities (or specific volumes), and the latent heat of vaporisation as functions of temperature. Figure 8 represents the saturated pressure as a function of the temperature and the crush granular pressure as a function of the initial diameter. In the latter, the abscissa scale is reversed as the initial diameter plays the inverse role of temperature. These curves have a similar behaviour and both have a higher physical limit which is the critical point. Indeed, the analogues of vapour, liquid, and supercritical fluid present at the critical point are, respectively, initial particles, fragmented mixture, and small initial particles that never fragment. The main difference is that the curve $P_{sat}(T)$ has a physical lower limit which is the triple point. For granular materials, no triple point exists and the crush granular pressure tends to zero when the initial diameter tends to infinity. A common form of the saturation pressure is the Antoine (1888) equation

$$\log_{10}(P_{sat}) = A - \frac{B}{T + C}.$$

For CO_2 , $A = 9.87$, $B = 957.37$, and $C = 14.32$ for P_{sat} expressed in Pa and T in K. This equation is the local approximation of a more complex formula linking saturation pressure and temperature. It combines liquid and gas equations of state under the constraints of mixture energy and mixture specific volume conservation, equal pressures, equal temperatures, and equal Gibbs free energy among the phases. The coefficients A, B, and C are found by fitting with a least square method the saturation data of CO_2 available at the NIST online library (<http://webbook.nist.gov/chemistry/>).

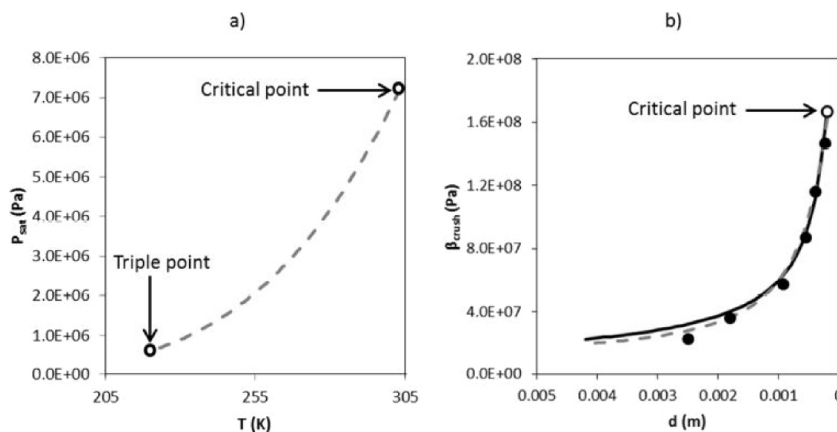


FIG. 8. (a) Saturation pressure of CO_2 as a function of the temperature. The Antoine equation corresponds to the grey dashed line. (b) Crush granular pressure as a function of the initial particles diameter. Experimental data are shown with black points. The Antoine-type relation is in the grey dashed line and the present fit, with Relation (1), corresponds to the black line. Critical and triple points (when existing) are represented by hollow circles in both (a) and (b).

Similar relation for the crush granular pressure as a function of initial particles diameter is considered

$$\log_{10}(\beta_{crush}) = A_1 - \frac{B_1}{d \times 10^6 + C_1}, \text{ with } \begin{cases} A_1 = 6.94 \\ B_1 = -1966, \beta_{crush} \text{ in Pa and } d \text{ in meters.} \\ C_1 = 1348 \end{cases}$$

Figure 8 shows the agreement between the Antoine-type relation and experimental data. However, that equation tends to a non-zero constant when the initial diameter tends to infinity. In the present context of granular materials, the Antoine relation seems consequently inappropriate. This is not surprising as its origins mentioned above, in particular temperature equilibrium among the phases cannot be transposed to granular materials.

To capture the asymptotic behaviour when the diameter tends to infinity, the following expression is used:

$$\beta_{crush}(d) = c_0 d^{c_1} \text{ with } \begin{cases} c_0 = 56.99 \times 10^4 \text{ Pa m}^{-c_1} \\ c_1 = -0.6738 \end{cases}. \quad (1)$$

Figure 9 shows fragmentation and saturation domes in the $(T-\rho)$ -plane and $(d-\rho)$ -plane, respectively. The dewpoint line and its analogue, the first fragmentation line, have similar behaviours. The bubble point line and the last fragmentation line behave differently near the critical point. In particular, no plateau is observed near this point for powders. As said earlier, another difference is the presence of the triple point for liquid-gas systems. Correlations for the saturation pressure as a function of the temperature exist in the literature (e.g., [Span and Wagner, 1996](#)). However, they require many parameters (eight to ten in that reference) to be accurate, in particular near the critical point. In the present work, the aim is to compare the two systems and derive simple relations for the granular one. As a result, a simpler correlation with three parameters only is used to link the crush volume fraction where the fragmentation appears as a function of initial particles diameter

$$\alpha_{crush,0}(d) = c_3(1 - e^{-c_4 d})^{c_5}, \text{ with } \begin{cases} c_3 = 0.605 \\ c_4 = 709 \text{ m}^{-1} \\ c_5 = -0.058 \end{cases}. \quad (2)$$

The analogue of this relation for CO₂ regarding the saturation density of vapour also gives satisfying results, except near the critical point (Figure 9),

$$\rho_{sat,0} = A_2(1 - e^{-B_2 T})^{C_2}, \text{ with } \begin{cases} A_2 = 1.23 \times 10^{11} \text{ kg/m}^3 \\ B_2 = 7.77 \times 10^{-4} \text{ K}^{-1} \\ C_2 = 12.67 \end{cases}.$$

The correlation used to fit the fragmentation end curve $\alpha_{crush,1}$ is

$$\alpha_{crush,1}(d) = c_6 + c_7 d + c_8 d^2, \text{ with } \begin{cases} c_6 = 0.68 \\ c_7 = 9.32 \text{ m}^{-1} \\ c_8 = 1.30 \times 10^4 \text{ m}^{-2} \end{cases}. \quad (3)$$

Another difference between liquid-vapour systems and powders is the (concave) bubble point line of Figure 9(a) while the “last fragmentation line” of Figure 9(b) is convex.

The critical point is now estimated as the intersection of the first and last fragmentation lines. For soda lime particles, the fragmentation critical point corresponds to

$$d_{critical} = 190 \times 10^{-6} \text{ m}, \alpha_{critical} = 0.682, \text{ and } \beta_{critical} = 183 \text{ MPa.}$$

The determination of the specific fragmentation energy as a function of the initial diameter is now addressed. It corresponds to the analogue of the latent heat of vaporisation. As the heat transfer is

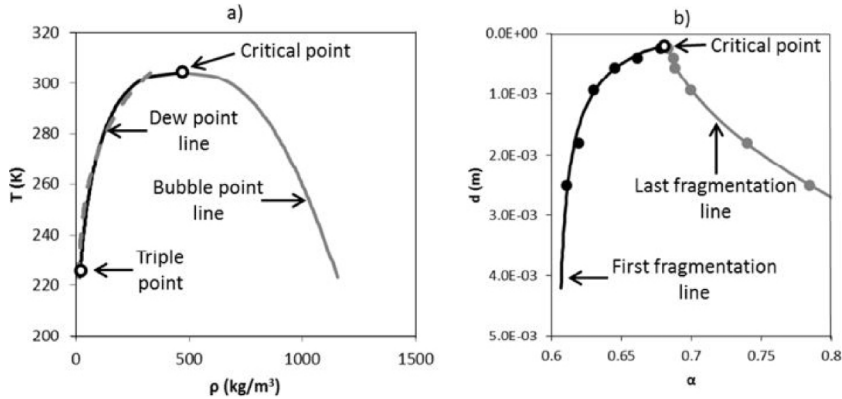


FIG. 9. (a) Saturation dome of CO₂ as a function of the density. The bubble point line is shown with black lines and the dew point line with grey lines. (b) Fragmentation dome as a function of the solid volume fraction. The first fragmentation line is shown with black points and the last fragmentation line is shown with grey points. For both (a) and (b), critical and triple points (when existing) are represented by hollow circles.

neglected during fragmentation, the related energy is determined as

$$E_{crush}(d) = - \int_{v_{crush,0}(d)}^{v_{crush,1}(d)} \beta dV,$$

with E_{crush} expressed in J/kg, β in Pa, and specific volumes $v_{crush,0}$ and $v_{crush,1}$ in m³/kg.

The specific volumes $v_{crush,0}$ and $v_{crush,1}$ represent, for a given particle diameter, the specific volumes where the fragmentation begins and ends (analogues of vapour and liquid saturation volumes). To compute the fragmentation energy, the crush granular pressure is used. For a given initial diameter, this pressure is constant during fragmentation and the related fragmentation energy reads

$$E_{crush}(d) = \beta_{crush}(d)(v_{crush,0}(d) - v_{crush,1}(d)).$$

Experimental data for $\Delta v_{crush}(d) = v_{crush,0}(d) - v_{crush,1}(d)$ are shown in Figure 10.

It remains to compute the specific fragmentation energy and two specific definitions may be considered in this aim. In the first definition, the total mass of powder is considered, yielding the specific energy per unit mass of initial powder (E_{crush}).

It can be divided by the mass fraction of the fragmented powder $Y_{frag} = \frac{m_{frag}}{m_{tot}}$ as only part of the powder sample is fragmented. Both definitions are considered in the graph (b) of Figure 11 where these energies are shown as functions of the particle diameter.

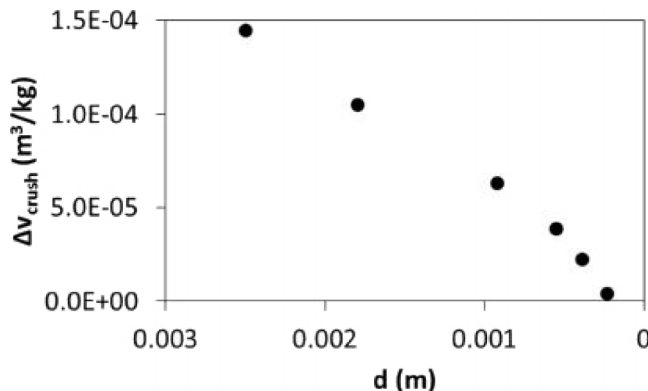


FIG. 10. Specific volume variations ($\Delta v_{crush}(d)$) of the soda lime granular bed during fragmentation as a function of the initial diameter.

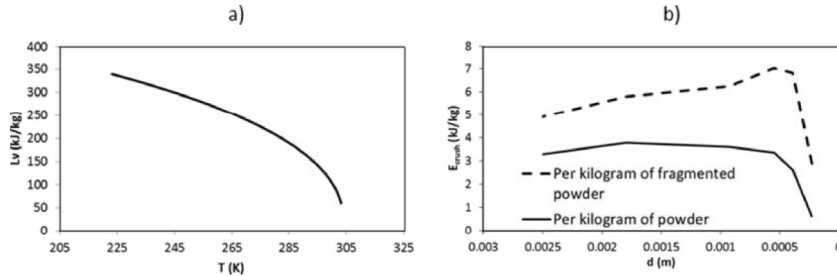


FIG. 11. (a) Specific latent heat of the vaporisation of CO_2 as a function of the temperature. (b) Specific crush energy as a function of the particles initial diameter.

Both definitions are useful. The first one, based on the unit mass of the initial powder, is needed for global computations, at the scale of granular beds. The second one provides information for fragmented particles and is more suitable for local computations, as done, for example, in [Antonyuk *et al.* \(2006\)](#) and [Moreno-Atanasio and Ghadiri \(2006\)](#).

Figure 11(b) provides extra information. It is often considered that the fragmentation energy is directly linked to the specific surface of the grains. Such dependence is absent in this figure as the fragmentation energy is nearly constant while the particle diameter varies by a factor 3, corresponding to a specific interfacial area of $1 \text{ m}^2/\text{kg}$ for the largest particles ($2500 \mu\text{m}$ initial diameter) to $3 \text{ m}^2/\text{kg}$ for those of $925 \mu\text{m}$ initial diameter. This remark supports the observations of [McSaveney and Davies \(2009\)](#).

It is also interesting to compare specific energies reported in Figure 11(b) to literature data. [Bergstrom *et al.* \(1961\)](#) reported a specific crush energy of about 2 kJ/kg for soda lime particles. The particles considered in this reference were significantly bigger than those considered in the present study, this difference explaining the shift in reported energies. [Jandacka *et al.* \(2009\)](#) considered mineral almandine powders and reported specific crush energies of about 3 kJ/kg . [Lade *et al.* \(1996\)](#) reported lower energy (about 0.6 kJ/kg) but were addressing softer materials (soils). Energy levels of Figure 11(b) seem in qualitative agreement with these data, in particular with those of [Bergstrom *et al.* \(1961\)](#).

A. Practical use of the graphs

As an engineering example of the present data use, let us consider a bumper aimed to stop a car of 1000 kg at velocity 198 km/h ($u = 55 \text{ m/s}$). The corresponding kinetic energy is 1513 kJ .

The initial powder grain size must be chosen in accordance to the impact pressure P_{impact} . Assuming sound speed c in the glass powder of the order of 300 m/s (estimated with Relation (6) and checked with [Rogue *et al.*, 1998](#) and [Hostler, 2004](#) data), the impact pressure is approximately given by

$$P_{\text{impact}} = P_{\text{atm}} + (\alpha\rho)cu = 10^5 + 0.6 \times 2500 \times 300 \times 55 \approx 25 \text{ MPa},$$

where $(\alpha\rho) = 0.6 \times 2500 = 1500 \text{ kg/m}^3$ denotes the density of the granular bed.

For such pressure level, Figure 8(b) indicates that particles must have a diameter greater than 3 mm . For these particles, the crush energy is about $E_{\text{crush}} \cong 3 \text{ kJ/kg}$. Thus 504 kg of glass powder made of 3 mm initial diameter spheres will be appropriate to dissipate the kinetic energy of the 1000 kg car impacting at 198 km/h .

IV. ERROR BAR AND INSTABILITIES

During the fragmentation process, instabilities appeared resulting in pressure oscillations having serious consequences on the error bar associated with pressure measurements. This phenomenon is clearly dominant compared to other sources of measurement uncertainties.

These instabilities appeared more intense for big particles. For Tests 1–4, the range of pressure oscillations and corresponding error bars are reported in Figure 12 and Table II. The mean value

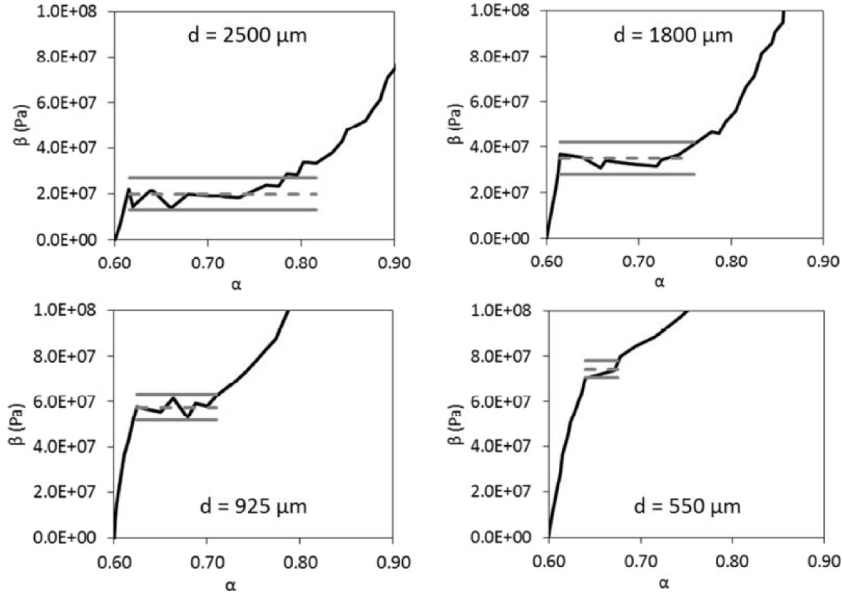


FIG. 12. Illustration of “metastable states” and associated pressure oscillations occurring during the fragmentation process for various initial particle sizes ($d = 2500, 1800, 925,$ and $550 \mu\text{m}$). Experimental compression curves are shown with black lines. The mean values of the fragmentation plateau are shown in dashed grey lines and the maximum deviations are shown in grey lines.

of the pressure plateau is represented in dashed grey lines and the maximum deviations are in grey lines in Figure 12. The maximum deviation decreases when the initial diameter decreases too.

For big particles (Test 1, for example), it seemed that the rupture of each individual particle emitted characteristic sound when breaking while inducing significant pressure oscillations. For Tests 5 and 6, dealing with small particles, such instabilities were not observed.

V. FRAGMENTATION DIAGRAM MODELLING

In this section, modelling of the fragmentation diagram is addressed. The aim is to reproduce this diagram in the (β, α) -plane (Figure 4(a)) with the help of an EOS expressing the crush granular pressure β as a function of the volume fraction and initial particle diameter. Two EOS are considered. The first one assembles piecewise functions while the second one mimics the van der Waals formulation.

A. Granular equation of state

In this section, we address the modelling of compaction curves with piecewise functions. In this frame, the granular pressure β is given by

$$\beta(\alpha, d) = \begin{cases} \beta_0(\alpha) & \text{if } \alpha < \alpha_{crush,0}(d) \\ \beta_{crush}(d) & \text{if } \alpha_{crush,0}(d) \leq \alpha \leq \alpha_{crush,1}(d) \\ \beta_1(\alpha, d) & \text{otherwise} \end{cases}, \quad (4)$$

TABLE II. Granular pressure deviation due to “metastable states” during the fragmentation process.

Mean grain size (μm)	2500	1800	925	550
Mean fragmentation pressure (MPa)	20	36	57	87
Maximum deviation (MPa)	± 7.0	± 7.2	± 5.7	± 4.35
Maximum deviation (%)	$\pm 35\%$	$\pm 20\%$	$\pm 10\%$	$\pm 5\%$

where $\alpha_{crush,0}$ and $\alpha_{crush,1}$ are the solid volume fractions crush bounds representing, respectively, the beginning and end of the fragmentation process. For a given powder, these bounds depend only on the initial diameter of the particles. β_0 represents the compaction curve before fragmentation and depends only on the volume fraction. β_{crush} corresponds to the crush granular pressure and depends only on the initial diameter. β_1 represents the post fragmentation compaction curve and depends both on the volume fraction and initial diameter. Figure 13 illustrates the preceding definitions, these functions being determined from the experimental data.

The analytical expressions of $\beta_{crush}(d)$, $\alpha_{crush,0}(d)$, and $\alpha_{crush,1}(d)$ were determined previously and correspond to Equations (1)–(3).

The compaction curves before fragmentation are now considered. Experimental observations indicate that these curves are independent of the initial particles diameter.

When dealing with solid-gas mixtures under compression, only the solid phase is subjected to intergranular efforts and as a consequence, contains configurational energy, representing the energy stored at particles contacts and deformed layers. The granular EOS is determined by the quasi-static compression of powders. The system volume is measured and the granular bed solid volume fraction is deduced, as a function of the applied constraint. This type of experiment is described, for example, in Kuo *et al.* (1980) and Elban and Chiarito (1986) and in the present work. Such measurements consequently summarize all three dimensional contacts and efforts and record their collective effects.

Compression curves (granular pressure versus solid volume fraction α) are fitted with the following function (Saurel *et al.*, 2010), representing the configuration energy (granular pressure will be expressed subsequently):

$$B(\alpha) = \tau B_0(\alpha)^n, \tag{5}$$

with

$$B_0(\alpha) = \begin{cases} (1 - \alpha) \ln(1 - \alpha) + (1 + \ln(1 - \alpha_0))(\alpha - \alpha_0) - (1 - \alpha_0) \ln(1 - \alpha_0), & \text{if } \alpha_0 < \alpha, \\ 0, & \text{otherwise} \end{cases},$$

where α_0 corresponds to the solid volume fraction when the granular constraint is zero ($\alpha_0 = 0.6$ in the present work). This volume fraction depends on the granular material, on its morphology, etc. It is clear in (5) that $B(\alpha_0) = 0$, ensuring the continuity of B at $\alpha = \alpha_0$. Parameters τ and n are the characteristics of a given powder and more precisely of its response to quasi-static loading. For soda lime, parameters associated with these functions are

$$\begin{cases} \tau = 415 \times 10^3 \text{ J/kg} \\ n = 1.001 \end{cases}.$$

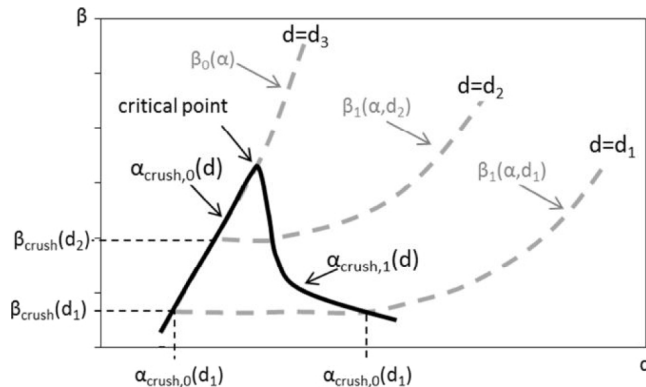


FIG. 13. Schematic representation of the “fragmentation diagram.”

For the present application, it is necessary to express the first and second derivatives of (5). The first derivative provides the granular pressure appearing in (4), defined by

$$\beta_0(\alpha) = (\alpha\rho) \frac{dB}{d\alpha} = \begin{cases} -(\alpha\rho) \tau n \ln\left(\frac{1-\alpha}{1-\alpha_0}\right) \left(\frac{B(\alpha)}{\tau}\right)^{\frac{n-1}{n}} & \text{if } \alpha > \alpha_0, \\ 0 & \text{otherwise} \end{cases},$$

with

$$\frac{dB(\alpha)}{d\alpha} = \tau n \frac{dB_0(\alpha)}{d\alpha} B_0(\alpha)^{n-1} \text{ and } \frac{dB_0(\alpha)}{d\alpha} = \ln\left(\frac{1-\alpha_0}{1-\alpha}\right).$$

The second derivative appears in the definition of the mechanical equilibrium mixture sound speed (Kapila *et al.*, 2001),

$$\rho_{mix} c_{mix}^2 = (\alpha\rho c^2 + (1-\alpha)\rho_g c_g^2) - \frac{(\rho c^2 - \beta_0 - \rho_g c_g^2)^2}{\frac{\rho c^2}{\alpha} + \alpha\rho \frac{d^2B}{d\alpha^2} + \frac{\rho_g c_g^2}{1-\alpha}}, \quad (6)$$

with

$$\frac{d^2B}{d\alpha^2} = \tau n \left(\frac{d^2B_0}{d\alpha^2} B_0^{n-1} + \left(\frac{dB_0}{d\alpha} \right)^2 (n-1) B_0^{n-2} \right) \text{ and } \frac{d^2B_0}{d\alpha^2} = \frac{1}{1-\alpha}.$$

In the present applications, gas phase effects can be neglected compared to solid and granular ones, yielding

$$c_{mix}^2 = c^2 - \frac{1}{\rho_{mix}} \frac{(\rho c^2 - \beta_0)^2}{\frac{\rho c^2}{\alpha} + \alpha\rho \frac{d^2B}{d\alpha^2}}.$$

Post fragmentation compaction curves are now addressed. These curves depend on the volume fraction and initial particles diameter. As this part is also a compaction process, we use the same mathematical form as β_0 with an additional function $F(d)$,

$$\beta_1(\alpha, d) = \begin{cases} -(\alpha\rho) \tau(d) n(d) \ln\left(\frac{1-\alpha}{1-\alpha_0(d)}\right) \left(\frac{B(\alpha)}{\tau(d)}\right)^{\frac{n(d)-1}{n(d)}} + F(d) & \text{if } \alpha > \alpha_0(d), \\ 0 & \text{otherwise} \end{cases}. \quad (7)$$

Now coefficients α_0 , τ and n are all functions of the initial diameter. When the fragmentation is done and compression continued, the new compaction curve starts at the end crush volume fraction $\alpha_{crush,1}(d)$. Thus $\alpha_0(d)$ becomes $\alpha_0(d) = \alpha_{crush,1}(d)$. In order to enforce the continuity of the compaction curve during and after fragmentation, function F must be equal to the crush pressure $F(d) = \beta_{crush}(d)$ given by Relation (1).

The various loading curves are then used to determine functions $\tau(d)$ and $n(d)$ yielding the following fittings:

$$\tau(d) = c_9 + c_{10}d, \text{ with } \begin{cases} c_9 = 116 \times 10^3 \text{ J/kg} \\ c_{10} = -3.420 \times 10^7 \text{ J/kg/m} \end{cases}, \quad (8)$$

$$n(d) = c_{11} + c_{12}d + c_{13}d^2 + c_{14}d^3, \text{ with } \begin{cases} c_{11} = 1.018 \\ c_{12} = 4.155 \times 10^2 \text{ m}^{-1} \\ c_{13} = -2.267 \times 10^5 \text{ m}^{-2} \\ c_{14} = 2.386 \times 10^7 \text{ m}^{-3} \end{cases}. \quad (9)$$

These relations are compared to the experimental data in Figure 14, showing good agreement.

Figure 15 shows the overall comparison between the experiments and the present EOS, based on Relations ((1)–(9)).

With the present formulation, the phase diagram is described by Systems (1)–(9). We now address the same goal with a unique formulation.

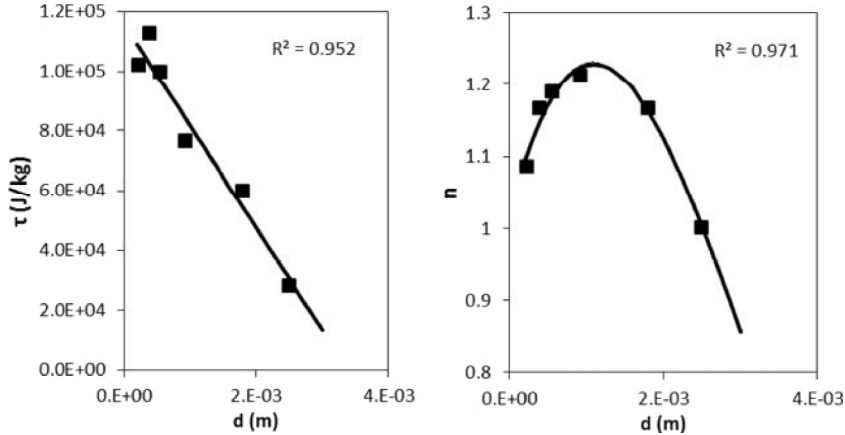


FIG. 14. Equation of state of crushed powders: (a) Function τ as a function of the initial diameter. (b) Function n as a function of the initial diameter. Experimental data are shown with square symbols.

B. van der Waals-type EOS

We now address the modelling of the fragmentation diagram with an EOS quite similar to the van der Waals one that reads

$$P(\rho, T) = \frac{\rho r T}{1 - b\rho} - a\rho^2,$$

where P , ρ and T represent, respectively, the pressure (Pa), density (kg/m^3) and temperature (K). $r = R/W$ with R the gas constant (in J/mol/K) and W the fluid molar weight (kg/mol). Constants a and b are the characteristics of a given fluid. They are determined knowing that $\left(\frac{\partial P}{\partial \rho}\right) = 0$ and $\left(\frac{\partial^2 P}{\partial \rho^2}\right) = 0$ at the critical point (van der Waals, 1873). These constraints yield $a = \frac{27r^2T_c^2}{64P_c}$ and $b = \frac{rT_c}{8P_c}$. For CO_2 , $T_c = 304.18$ K and $P_c = 73.80 \times 10^5$ Pa (Suehiro *et al.*, 1996). As a result, we found $a = 188.8$ Pa m^6/kg^2 and $b = 9.735 \times 10^{-4}$ m^3/kg . Tabulated data from the NIST library (<http://webbook.nist.gov/chemistry/>) and van der Waals EOS for CO_2 are reported in Figure 16, showing qualitative agreement only. The van der Waals formulation predicts metastable states, not reported in tabulated data but present in reality. It also appears that the phase transition density range differs noticeably. Many authors have proposed enhanced versions of the van der Waals formulation by modifying either the attractive and repulsive terms (Redlich and Kwong, 1949; Peng and Robinson, 1976; Patel and Teja, 1982; and Reiss *et al.*, 1959). In the present work, the aim is to represent the fragmentation phase diagram with as simple an EOS as possible.

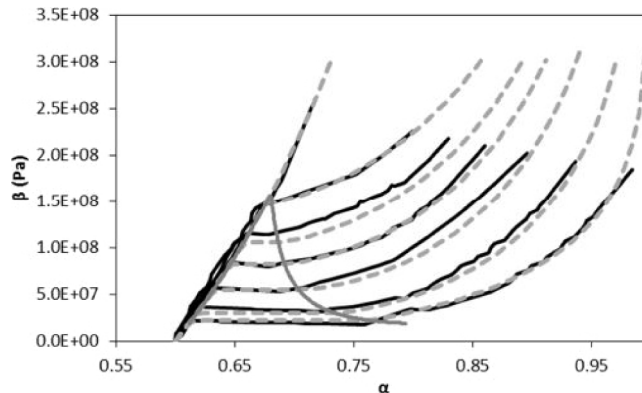


FIG. 15. (β, α) -crush diagram of the soda lime glass powder. Experiments are shown in black lines and computations in dash grey lines. The computed fragmentation dome is represented by the continuous grey line.

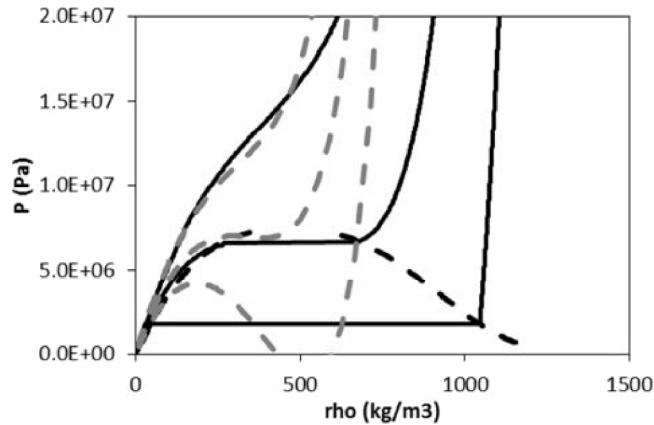


FIG. 16. Comparison between the tabulated pressure (grey lines) for CO₂ and computed pressure using van der Waals EOS (dashed grey lines) as a function of the density for 250, 300, and 350 K.

In this direction, some differences between the liquid-vapour phase change and fragmentation process must be pointed out. For a gas, following an isotherm, the pressure increases slowly as a function of the density while the pressure of the liquid increases stiffly. Opposite behaviour is observed for the fragmentation process with respect to the granular pressure evolution as a function of the solid volume fraction. Furthermore, the density starts near zero for fluids while the apparent solid initial density is of the order of 1000 kg/m³ when the granular pressure appears. Indeed particles crush-up starts and ends with solid particles.

In order to have similar qualitative behaviour between the fragmentation curves and the liquid-vapour phase change curves, a new scaling is considered given the following constraints:

1. Let us define the rescaled volume fraction α^* such that the variation range $[\alpha_0, 1]$ becomes $[0, \alpha_{\max}^*]$ where α_{\max}^* represents a constant to define.
2. The new scale must decrease the granular pressure slope for small α^* .
3. The new scale must increase the granular pressure slope for large α^* .

Given these constraints, the following scaling function was chosen:

$$\alpha^* = c_{15}(1 - e^{-c_{16}(\alpha - \alpha_0)}). \quad (10)$$

In order to qualitatively match the experimental fragmentation curves (as done for CO₂), the following additional constraints have been added:

1. $\alpha_{\max}^* \approx 1000$ (maximal value of the rescaled volume fraction),
2. $\alpha_{\text{crit}}^* \approx 500$ (value of the critical point volume fraction).

Given these constraints, the constants c_{15} and c_{16} are deduced as $c_{15} = 1000$ and $c_{16} = 10$ (corresponding to $\alpha_{\max}^* = 981$ and $\alpha_{\text{crit}}^* \approx 555$).

Typical pressure record is shown in Figure 17 as a function α and α^* .

The granular van der Waals EOS in consideration now reads

$$\beta(\alpha, d) = \frac{c(d)\alpha^*}{1 - b\alpha^*} - a(\alpha^*)^2, \quad (11)$$

where $c(d)$ is the analogue of rT and is therefore a function of the initial particles diameter.

In Fig. 18(b), the curve fitting was addressed with parameters $c = 2.1 \cdot 10^5$ Pa, $b = 7.9 \cdot 10^{-4}$, and $a = 6 \cdot 10^{-2}$ Pa, but it appeared impossible to capture both the plateau and post fragmentation compaction curve, as shown in Figure 18.

To correct this weakness, the quadratic term of the van der Waals EOS is changed to a cubic one and an exponent is added to the short distances repulsive term,

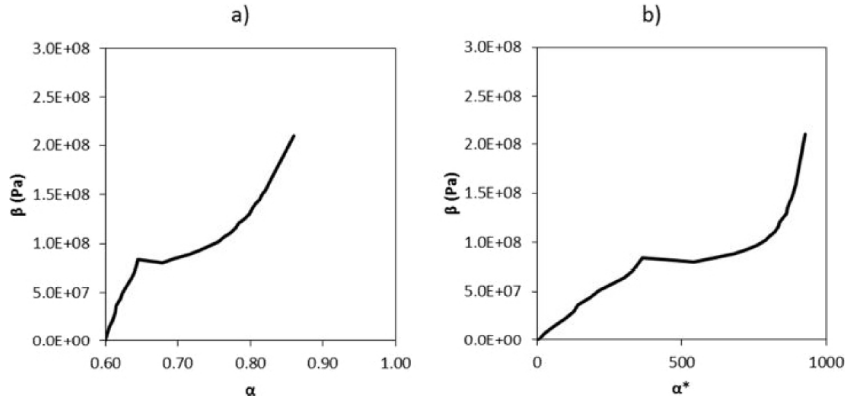


FIG. 17. Granular pressure record for a granular bed of soda lime with particles of 0.5–0.6 mm diameter as a function of the (a) volume fraction α and (b) rescaled one α^* .

$$\beta(\alpha, d) = \frac{c(d)\alpha^*}{(1 - b\alpha^*)^{0.41}} - a(\alpha^*)^3. \tag{12}$$

Doing so, attractive effects are increased while short distance repulsive ones are decreased. There is no particular physical relevance in these changes, just an attempt to improve the curve fitting of Figure 18(b). With these modifications improved agreement is found with the following parameters $a = 4.50 \times 10^{-1}$ Pa, $b = 1.00 \times 10^{-3}$ and $c = 2.12 \times 10^5$ Pa as shown in Figure 18.

The agreement being better with the formulation (12) we now address the determination of c as a function of the initial particle size d . Parameters a and b are kept constant and $c(d)$ is determined for each curve using the least square method. Figure 19 represents the evolution of function c versus initial diameter.

For the initial diameter smaller than the critical one ($d < d_{crit}$), function $c(d)$ is constant as no fragmentation appears and all compression curves are superimposed, independently of the particle size. In order to fit the previous dataset, several functions have been considered and the following formulation with three parameters only was retained:

$$c(d) = \begin{cases} c_{17}[1 - \exp(-c_{18}d)]^{c_{19}} & \text{if } d > d_{crit} \\ c_{17}[1 - \exp(-c_{18}d_{crit})]^{c_{19}} & \text{otherwise} \end{cases}, \text{ with } \begin{cases} c_{17} = 136.9 \times 10^3 \text{ Pa} \\ c_{18} = 910.8 \text{ m}^{-1} \\ c_{19} = -0.499 \end{cases}. \tag{13}$$

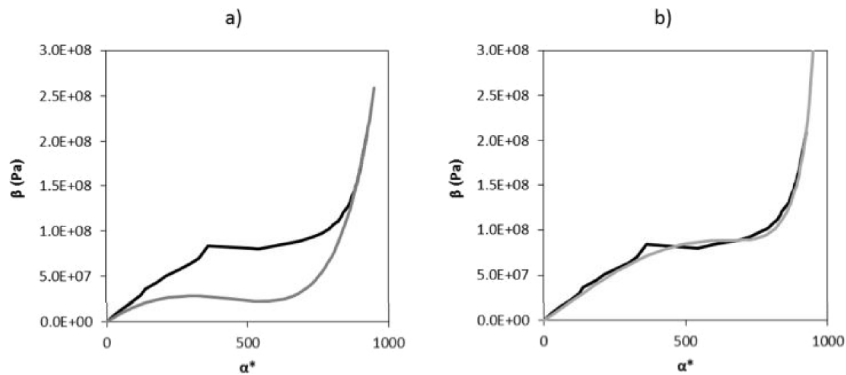


FIG. 18. Granular pressure as a function of α^* , comparison of the various theoretical formulations for a granular bed with the given initial particle size. Experimental data are shown in black lines, van der Waals approximation (11) is shown with grey lines in (a), and formulation (12) is shown with grey line in (b), putting in evidence improvements.

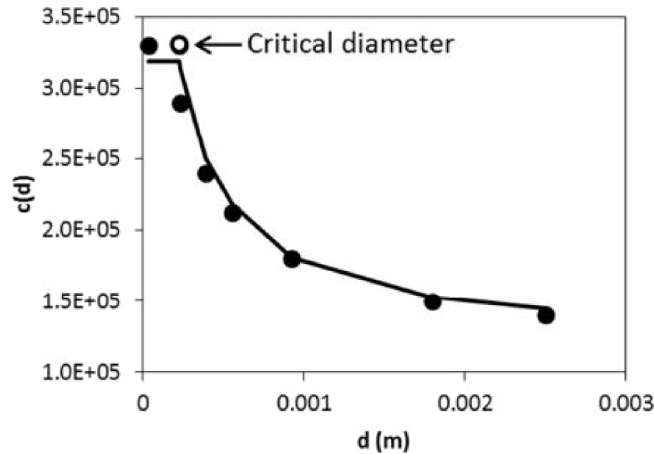


FIG. 19. Function $c(d)$: Experiments are shown with dot symbols and curve fit with lines. The critical point is represented by a hollow circle.

It enables to capture both the stiff slope of $c(d)$ when $d \rightarrow d_{crit}^+$ and the decreasing slope of $c(d)$ when $d \rightarrow 0.003$ m. Figure 20 compares the experimental data and computations with function $c(d)$ given by (13).

The modified van der Waals EOS (12) is qualitatively in good agreement with the experiments. However, as for the original van der Waals formulation, negative pressures appear in Figure 20. Negative pressures (tensions) may occur in pure liquids, under specific conditions (Brin, 1956). In dry granular media, this is clearly impossible, as the presence of gas preserves the pressure positivity. The van der Waals type formulation can thus be used as an approximation of the pre- and post-fragmentation states, not the “phase-transition zone.” It thus appears that the various van der Waals type formulations examined in the present study are inappropriate to model the phase diagram of crushed powders. This is related to the non-convexity of van der Waals type EOS (Menikoff and Plohr, 1989 and Saurel *et al.*, 2008) in the crush zone. The physics of granular material under breakage conditions differs significantly from the liquid-vapour phase change, as already mentioned with respect to the Antoine relation. Variants of the van der Waals EOS (Redlich and Kwong, 1949; Peng and Robinson, 1976; Patel and Teja, 1982; and Reiss *et al.*, 1959) are no more convex and consequently seem inappropriate as well.

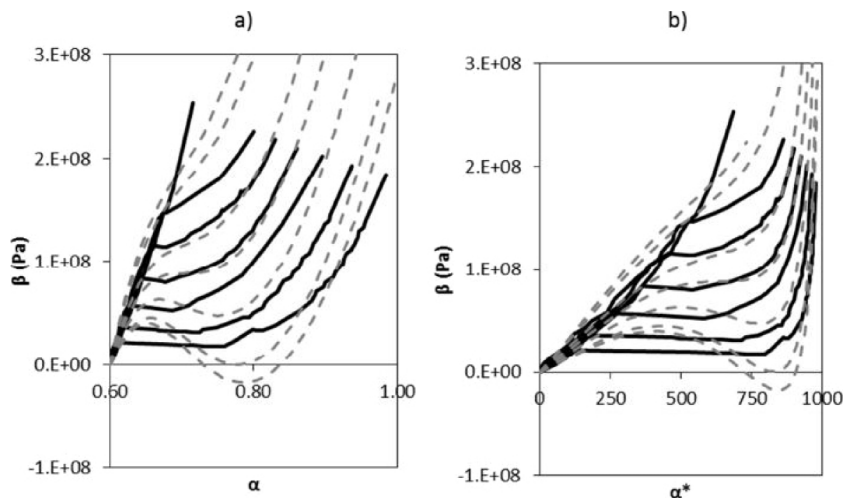


FIG. 20. Experimental data (black lines) and EOS (12) (dashed grey lines). (a) Plot in the (β, α) -plane. (b) Plot in the (β, α^*) -plane.

VI. CONCLUSIONS

The analogue of the liquid-vapor phase diagram has been determined for granular beds made of quasi-monodisperse spherical particles. Under compression effects, particles fragment and form a mixture (in the general sense) made of initial particles and fragments. This “phase transition” process occurs at a precise pressure for a given initial particle size. The energy needed to fragment the bed varies as a function of the particle size. The corresponding crush diagram contains relevant information and is determined on the basis of simple experiments.

Model equations of state have been examined to reproduce the crush diagram. Accurate representation has been obtained with assembled piecewise functions while van der Waals type formulations appeared inappropriate.

Many perspectives can be considered to continue these investigations with,

1. study of time dependence and relaxation time to equilibrium,
2. the influence of temperature on crush-up,
3. the building of a flow model containing such phase transition process.

ACKNOWLEDGMENTS

The authors are grateful to the anonymous referees who helped to improve significantly the quality of the manuscript.

- Antoine, C., “Tensions des vapeurs: Nouvelle relation entre les tensions et les températures,” *C. R. Seances Acad. Sci. (in French)* **107**, 681–684 (1888).
- Antonyuk, S., Khanal, M., Tomas, J., Heinrich, S., and Mörl, L., “Impact breakage of spherical granules: Experimental study and DEM simulation,” *Chem. Eng. Process.: Process Intensif.* **45**(10), 838–856 (2006).
- Bdzil, J. B., Menikoff, R., Son, S. F., Kapila, A. K., and Stewart, D. S., “Two-phase modeling of deflagration-to-detonation transition in granular materials: A critical examination of modeling issues,” *Phys. Fluids* **11**(2), 378–402 (1999).
- Bergstrom, B. H., Sollenberger, C. L., and Mitchell, Jr., W., “Energy aspects of single particle crushing,” *Trans. AIME* **220**, 367–372 (1961).
- Brin, A. Y., “Contribution à l’étude de la couche capillaire et de la pression osmotique,” Ph.D. dissertation (Univ. Paris, Paris, 1956).
- Davison, L., Grady, D. E., and Shahinpoor, M., *High-Pressure Shock Compression of Solids. II: Dynamic Fracture and Fragmentation* (Springer Science & Business Media, 2012).
- Desmond, K. W. and Weeks, E. R., “Influence of particle size distribution on random close packing of spheres,” *Phys. Rev. E* **90**, 022204 (2014).
- Einav, I., “Breakage mechanics—Part I: Theory,” *J. Mech. Phys. Solids* **55**, 1274–1297 (2007a).
- Einav, I., “Breakage mechanics—Part II: Modelling granular materials,” *J. Mech. Phys. Solids* **55**, 1298–1320 (2007b).
- Elban, W. and Chiarito, M., “Quasi-static compaction study of coarse HMX explosive,” *Powder Technol.* **46**(2–3), 181–193 (1986).
- Fortov, V. E., Altshuler, L. V., Trunin, R. F., and Funtikov, A. I., *High-Pressure Shock Compression of Solids VII: Shock Waves and Extreme States of Matter* (Springer, 2013).
- Griffith, A. A., “The phenomena of rupture and flow in solids,” *Philos. Trans. R. Soc., A* **221**, 163–198 (1921).
- Hall, E. O., “The deformation and ageing of mild steel: III discussion of results,” *Proc. Phys. Soc., London, Sect. B* **64**, 747–753 (1951).
- Hostler, S. R., “Wave propagation in granular materials,” Ph.D. dissertation (California Institute of Technology, 2004).
- Jandacka, P., Hlavac, L. M., Madr, V., Sancer, J., and Stanek, F., “Measurement of specific fracture energy and surface tension of brittle materials in powder form,” *Int. J. Fract.* **159**(1), 103–110 (2009).
- Kapila, A. K., Menikoff, R., Bdzil, J. B., Son, S. F., and Stewart, D. S., “Two-phase modeling of deflagration-to-detonation transition in granular materials: Reduced equations,” *Phys. Fluids* **13**(10), 3002–3024 (2001).
- Kuo, K. K., Yang, V., and Moore, B. B., “Intragranular stress, particle-wall friction and speed of sound in granular propellant beds,” *J. Ballist.* **4**(1), 697–730 (1980).
- Lade, P. V., Yamamuro, J. A., and Bopp, P. A., “Significance of particle crushing in granular materials,” *J. Geotech. Eng.* **122**(4), 309–316 (1996).
- Marsh, S. P., *LASL Hugoniot Data* (University of California Press, 1980).
- Menikoff, R. and Plohr, B. J., “The Riemann problem for fluid flow of real materials,” *Rev. Mod. Phys.* **61**(1), 75 (1989).
- Mott, N. F., “Fracture of metals: Theoretical considerations,” *Eng. Fract. Mech.* **165**(4275), 16–18 (1948).
- Mott, N. F., “Fragmentation of shell casings and the theory of rupture in metals,” in *Fragmentation of Rings and Shells* (Springer Berlin Heidelberg, 2006), pp. 295–325.
- McSaveney, M. J. and Davies, T. R., “Surface energy is not one of the energy losses in rock comminution,” *Eng. Geol.* **109**(1), 109–113 (2009).
- Moreno-Atanasio, R. and Ghadiri, M., “Mechanistic analysis and computer simulation of impact breakage of agglomerates: Effect of surface energy,” *Chem. Eng. Sci.* **61**(8), 2476–2481 (2006).

- National Institute of Standard and Technology (NIST), Chemistry WebBook, <http://webbook.nist.gov/chemistry/>.
- Passman, S. L., Nunziato, J. W., and Walsh, E. K., *A Theory of Multiphase Mixtures* (Springer, New York, 1984), pp. 286–325.
- Patel, N. C. and Teja, A. S., “A new cubic equation of state for fluids and fluid mixtures,” *Chem. Eng. Sci.* **37**, 463–473 (1982).
- Peng, D. Y. and Robinson, D. B., “A new two-constant equation of state,” *Ind. Eng. Chem. Fundam.* **15**, 59–64 (1976).
- Petch, N. J., “The cleavage strength of polycrystals,” *J. Iron Steel Inst., London* **173**, 25–28 (1953).
- Redlich, O. and Kwong, J. N. S., “On the thermodynamics of solutions. V. An equation of state. Fugacities of gaseous solutions,” *Chem. Rev.* **44**, 233–244 (1949).
- Reiss, N. R., Frisch, H. L., and Lebowitz, J. L., “Statistical mechanics of rigid spheres,” *J. Chem. Phys.* **31**, 369–380 (1959).
- Rogue, X., Rodriguez, G., Haas, J. F., and Saurel, R., “Experimental and numerical investigation of the shock-induced fluidization of a particles bed,” *Shock Waves* **8**(1), 29–45 (1998).
- Saurel, R., Petitpas, F., and Abgrall, R., “Modelling phase transition in metastable liquids: Application to cavitating and flashing flows,” *J. Fluid Mech.* **607**, 313–350 (2008).
- Saurel, R., Favrie, N., Petitpas, F., Lallemand, M. H., and Gavriluk, S. L., “Modelling dynamic and irreversible powder compaction,” *J. Fluid Mech.* **664**, 348–396 (2010).
- Span, R. and Wagner, W., “A new equation of state for carbon dioxide covering the fluid region from the triple-point temperature to 1100 K at pressures up to 800 MPa,” *J. Phys. Chem. Ref. Data* **25**, 1509–1596 (1996).
- Suehiro, Y., Nakajima, M., Yamada, K., and Uematsu, M., “Critical parameters of $\{x\text{CO}_2 + (1 - x)\text{CHF}_3\}$ for $x = (1.0000, 0.7496, 0.5013, \text{ and } 0.2522)$,” *J. Chem. Thermodyn.* **28**, 1153–1164 (1996).
- van der Waals, J. D., “On the continuity of the gaseous and liquid states,” Ph.D. dissertation (University of Leiden, Leiden, 1873).